crystals

MDPI

Article

Oxalic Acid, a Versatile Coformer for Multicomponent Forms with 9-Ethyladenine

Mónica Benito [1,*], Miquel Barceló-Oliver [2], Antonio Frontera [2] and Elies Molins [1,*]

[1] Institut de Ciència de Materials de Barcelona (ICMAB-CSIC), Campus de la Universitat Autònoma de Barcelona, 08193 Bellaterra, Spain
[2] Departament de Química, Universitat de les Illes Balears, Ctra. Valldemosa km 7.5, 07122 Palma de Mallorca, Spain; miquel.barcelo@uib.es (M.B.-O.); toni.frontera@uib.es (A.F.)
* Correspondence: mbenito@icmab.es (M.B.); elies.molins@icmab.es (E.M.)

Abstract: Six new multicomponent solids of 9-ethyladenine and oxalic acid have been detected and characterized. The salt screening has been performed by mechanochemical and solvent crystallization processes. Single crystals of the anhydrous salts in 1:1 and 2:1 nucleobase:coformer molar ratio were obtained by solution crystallization and elucidated by single-crystal X-ray analysis. The supramolecular interactions observed in these solids have been studied using density functional theory (DFT) calculations and characterized by the quantum theory of "atoms in molecules" (QTAIM) and the noncovalent interaction plot (NCIPlot) index methods. The energies of the H-bonding networks observed in the solid state of the anhydrous salts in 1:1 and 2:1 nucleobase:coformer are reported, disclosing the strong nature of the charge assisted NH···O hydrogen bonds and also the relative importance of ancillary C–H··O H-bonds.

Keywords: nucleobases; multicomponent solids; crystal engineering; DFT; H-bonding

Citation: Benito, M.; Barceló-Oliver, M.; Frontera, A.; Molins, E. Oxalic Acid, a Versatile Coformer for Multicomponent Forms with 9-Ethyladenine. *Crystals* **2022**, *12*, 89. https://doi.org/10.3390/cryst12010089

Academic Editor: Josep Lluís Tamarit

Received: 10 December 2021
Accepted: 5 January 2022
Published: 10 January 2022

1. Introduction

The preparation of alternative salts, and more recently cocrystals, of many active pharmaceutical ingredients (APIs) has gained great attention as an important strategy in crystal engineering for the last decades. The use of salts and cocrystals for improving the physico-chemical properties of APIs has been demonstrated, as these solids can modify the solubility or dissolution rate, or even improve the physical stability. Around a half of the marketed products are estimated to be sold as salt forms [1]. Oxalic acid is among the different salt-forming acids listed for this purpose. It belongs to the second class of salt formers according to the *Handbook of Pharmaceutical Salts: Properties, Selection and Use* [1], as they are not naturally occurring but during their application have shown low toxicity and good tolerability. Through a search in the FDA Orange Book Database, we found only two approved examples, which are the specialty dosage forms commercialized as Lexapro® and Movantik®. The first one, in the market since 2009, is used for the treatment of depression and anxiety. Interestingly, it is not a classical salt, but in fact it is a hydrated cocrystal of a salt, composed of protonated escitalopram cations, oxalate dianions, unprotonated oxalic acid molecules and water molecules [2]. The second dosage form contains naloxegol oxalate, indicated for the treatment of opioid-induced constipation in adults with chronic non-cancer pain. Curiously, it was found through a small-scale screening due to the difficulties in preparing naloxegol in solid form [3]. As a result, two polymorphic forms were described, and the crystal structure resolution of Form B showed that it contained hydrogen oxalate anions [4]. In spite of the low incidence of oxalic acid in the list of the most used anions in APIs [5], many other examples have also been described in the literature exhibiting the interest of the scientific community for this coformer [6–9].

Among pharmaceutical compounds, nucleobases are of great value thanks to their contribution as structural components of several pharmaceuticals as well as for their

biological function as part of DNA and RNA. Very recently, a new cytosine derivative has been announced for COVID-19 oral treatment, molnupiravir [10].

After a careful revision of cocrystals or salts between oxalic acid and nucleobases or related compounds only a few examples resulted. These include pure adenine [11], N^6-benzyladenine [12], or the following xanthines: caffeine [13,14], theobromine [15] and theophylline [16,17]. The only example described as a cytosine derivative was for the antiretroviral compound, lamivudine [9].

9-Ethyladenine (9ETADE) is a modified nucleobase with the amino group at N(9) blocked by an ethyl chain (Scheme 1a). We have previously reported the ability of this modified nucleobase to form different salts and/or cocrystals with alkyl dicarboxylic acids (HOOC-X_n-COOH, with n from 1 to 4) as coformers depending on the ΔpK_a [18]. Now, as a continuation of our work related to this modified purine, we describe herein the special situation with oxalic acid. This is the most acidic (pK_a = 1.19) and shortest alkyl dicarboxylic acid we have studied but the most versatile and promiscuous in rendering several solid forms.

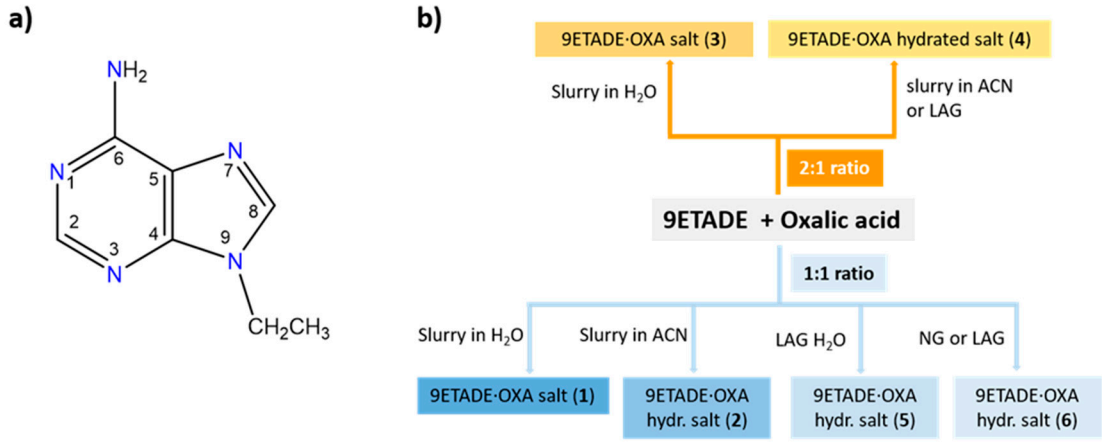

Scheme 1. (**a**) Molecular structure of 9-ethyladenine with numbering and (**b**) compounds of 9-ethyladenine with oxalic acid prepared in this work.

Herein, we present several multicomponent forms obtained by combination of the model compound 9-ethyladenine and oxalic acid, which have been prepared by solvent/slurry crystallization or mechanochemistry (liquid assisted grinding (LAG) or neat grinding (NG)) and their full characterization. The crystal structures of the two anhydrous salts have been solved. Moreover, density functional theory (DFT) calculations were used to understand/study their supramolecular interactions focusing on the energetics of the H-bonds, which were computed by carrying out a topological analysis of the electron density.

2. Materials and Methods

2.1. Materials

All reagents were purchased from Sigma-Aldrich Co. (Merck KGaA, Darmstadt, Germany) and used without further purification. Analytical grade solvents were used for the crystallization experiments. 9-Ethyladenine (9ETADE) was obtained as previously described by some of us [19].

2.2. Syntheses of Multicomponent Solids

Solution syntheses. In general, mixtures of 9ETADE and oxalic acid dihydrate in 1:1 or 2:1 molar ratio were suspended in Milli-Q water (for **1** and **3**) or in acetonitrile (for **2** and **4**) at room temperature for two days. After that, the solids were filtered and air-dried. Additional detailed data are included in Supplementary Information (SI).

Grinding Screening. As a general method, mechanochemical syntheses of the new compounds were performed using a Retsch MM400 mixer mill (Retsch, Haan, Germany) in 10 mL

agate grinding jars with two 5 mm agate balls. Mixtures containing 1:1 or 2:1 stoichiometric molar ratio of 9ETADE and oxalic acid dihydrate and the selected solvent were ground for 30 min at 30 Hz. Additional details are included in Supplementary Information (SI).

2.3. Characterization

Powder X-ray Diffraction (PXRD). PXRD data were collected using a Siemens D5000 powder X-ray diffractometer (Siemens, Munich, Germany) with Cu-Kα radiation (λ = 1.5418 Å), with 35 kV and 45 mA voltage and current applied. An amount of powder was gently pressed on a glass slide to afford a flat surface and then analyzed. The samples were scanned in the 2θ range of 2–50° using a step size of 0.02° and a scan rate of 1 s/step.

Single Crystal X-ray Diffraction (SC-XRD). Suitable crystals of **1** and **3** were selected for X-ray single crystal diffraction experiments, covered with oil (Infineum V8512, formerly known as Paratone N) and mounted at the tip of a nylon CryoLoop on a BRUKER-NONIUS X8 APEX-II KAPPA CCD diffractometer (Bruker, Karlsruhe, Germany) using graphite monochromated MoKα radiation (λ = 0.7107 Å). Crystallographic data were collected at 300 (2) K. Data were corrected for Lorentz and polarization effects and for absorption by SADABS [20]. The structural resolution procedure was made using the WinGX package [21]. The structure factor phases were solved by SHELXT-2014/5 or SHELXT-2018/2 [22]. For the full matrix refinement SHELXL-2017/1 or SHELXL2018/3 was used [23]. The structures were checked for higher symmetry with help of the program PLATON [24]. H-atoms were introduced in calculated positions and refined riding on their parent atoms, except for the protonation sites (H1A and H1B).

In Table 1 general and crystallographic data for the two new salts described are summarized.

Table 1. Crystallographic data and refinement for salts **1** and **3**.

Crystal	**1**	**3**
Empirical Formula	$C_9H_{11}N_5O_4$	$C_8H_{10}N_5O_2$
*M*r	253.23	208.21
Crystal system	Triclinic	Monoclinic
Space group	$P\,\bar{1}$	$P2_1/c$
a/Å	5.5478 (19)	10.325 (4)
b/Å	9.413 (3)	7.0783 (3)
c/Å	11.535 (4)	13.207 (5)
α/°	70.272 (5)	90
β/°	87.851 (5)	106.457 (5)
γ/°	81.231 (6)	90
V/Å^3	560.3 (3)	925.6 (6)
Z	2	4
Radiation type	Mo K$_\alpha$	Mo K$_\alpha$
μ/mm^{-1}	0.121	0.113
Temperature/K	300 (2)	300 (2)
Crystal size/mm	0.500 × 0.230 × 0.180	0.390 × 0.120 × 0.080
D_{calc}/g·cm^{-3}	1.501	1.494
Reflections collected	6719	1676
Independent Reflections	2581 [R(int) = 0.0277]	1676 [R(int) = 0.062]
Completeness to theta = 24.996°	99.8%	99.2%
F(000)	264	436
Data/restraints/parameters	2581/0/170	1676/0/140
Goodness-of-fit	1.056	1.090
Final R indices [I < 2d(I)]	R1 = 0.0420, wR2 = 0.1147	R1 = 0.0610, wR2 = 0.1465
R indices (all data)	R1 = 0.0478, wR2 = 0.1192	R1 = 0.0863, wR2 = 0.1540
Largest diff. peak and hole/e·Å^{-3}	0.318 and −0.222	0.235 and −0.275
CCDC nº	2126070	2126069

Thermogravimetric analysis—Differential scanning calorimetry (TGA-DSC). A simultaneous thermogravimetric analysis (TGA)—differential scanning calorimetry/differential thermal analysis (heat flow DSC/DTA) system NETZSCH -STA 449 F1 Jupiter (NETZSCH, Selb, Germany) was used to perform thermal analysis on the solids. Samples (3–8 mg) were placed in open alumina pan and measured at a scan speed of 10 °C min^{-1} from ambient temperature to 250 °C under N_2 atmosphere as protective and purge gas (their respective flow velocities were 20 and 40 mL/min).

Attenuated Total Reflection Fourier Transform Infrared spectroscopy (ATR-FT-IR). A Jasco 4700LE spectrophotometer (JASCO, Tokyo, Japan) with attenuated total reflectance accessory was used to record the FT-IR spectra of 9ETADE, oxalic acid dihydrate and the new compounds prepared in this work in the range from 4000 to 400 cm^{-1} and at a resolution of 4.0 cm^{-1}.

Determination of approximate solubilities. The approximate solubilities of the anhydrous 9ETADE salts were determined by the gravimetric method following the procedure described in [25,26]. To sum up, in a vial, an amount of solid (ca. 40–50 mg) was added a determined volume of Milli-Q water to obtain a supersaturated solution at room temperature. The suspensions were stirred for 2 h and then the agitation was stopped to allow slow settling of the solids in excess for at least 24 h. Samples of the supernatant liquid were taken using a syringe and filter via a nylon syringe filter (0.22 µm). The clear solutions were added to a pre-weighted vial (m_1) and the vial was weighted again (m_2). The solvent was allowed to evaporate in the fume hood until dry and the mass was recorded (m_3). The solids were dried in an oven at 30 °C under vacuum for 2 h to confirm no further weight decrease. The solubility was calculated as the amount of solid recovered ($m_3 - m_1$) divided by the volume of the solution ($m_2 - m_3$). The given values are the median of three replicates. The residual solids which did not dissolve were analyzed by PXRD to check the stability of the salts.

2.4. Stability Studies

Stability studies in solution. Mixtures of 9ETADE and oxalic acid in 1:1 ratio and using Milli-Q water or acetonitrile as a solvent were conducted at room temperature at different times (2, 24 and 48 h) to follow phase evolution.

Physical stability in solid state. The physical stability of the two anhydrous salts was carried out by exposing the solids to the certain range of relative humidity (RH). The humidity inside the chamber/desiccator was maintained at 75% RH using a sodium chloride saturated salt solution [27]. The samples were exposed for one week at 40 °C and 1 month at room temperature and subsequentially analyzed by PXRD.

2.5. Theoretical Calculations

Gaussian-16 [28] program package was used for the calculations reported in this work. For the energies and wavefunction calculations we have used the PBE0 [29] functional in combination with Grimme's dispersion correction (D3) [30] and the triple-ζ basis set def2-TZVP [31]. The molecular electrostatic potential (MEP) surfaces have been computed at the same level of theory and using the 0.001 a.u. isosurface to emulate the van der Waals surface. The experimental crystallographic coordinates have been used to evaluate the interactions in the solid state. This level of theory and methodology was used before to investigate similar interactions [32–35]. The Bader's quantum theory of "Atoms in molecules" (QTAIM) [36] and the noncovalent interaction index (NCIPlot) index [37] methods were used to characterize the hydrogen bonding interactions by means of the AIMall program [38]. The dissociation energies of the H-bonding interactions have been evaluated using the methodology proposed by Espinosa et al. [39] based on the potential energy density (Vr) at the bond critical points (CPs).

3. Results and Discussion

3.1. Solid-State Characterization of the Solids Obtained from Slurry or Mechanochemical Methods

The cocrystallization of 9-ethyladenine and oxalic acid was carried out in 1:1 or 2:1 (9ETADE:OXA) molar ratios. On the one hand, by mechanochemical process by neat grinding (NG) or liquid-assisted grinding (LAG), which have previously demonstrated to be fast methods for salt/cocrystal screenings. On the other hand, slurry experiments in water or acetonitrile were also performed with the purpose to check whether other plausible solid forms or solvates were possible. In solution, we found that for these two molar ratios and the two solvents, up to four different powder patterns were obtained (see Figure 1). The solids were identified as shown in Scheme 1b (compounds **1**–**4**).

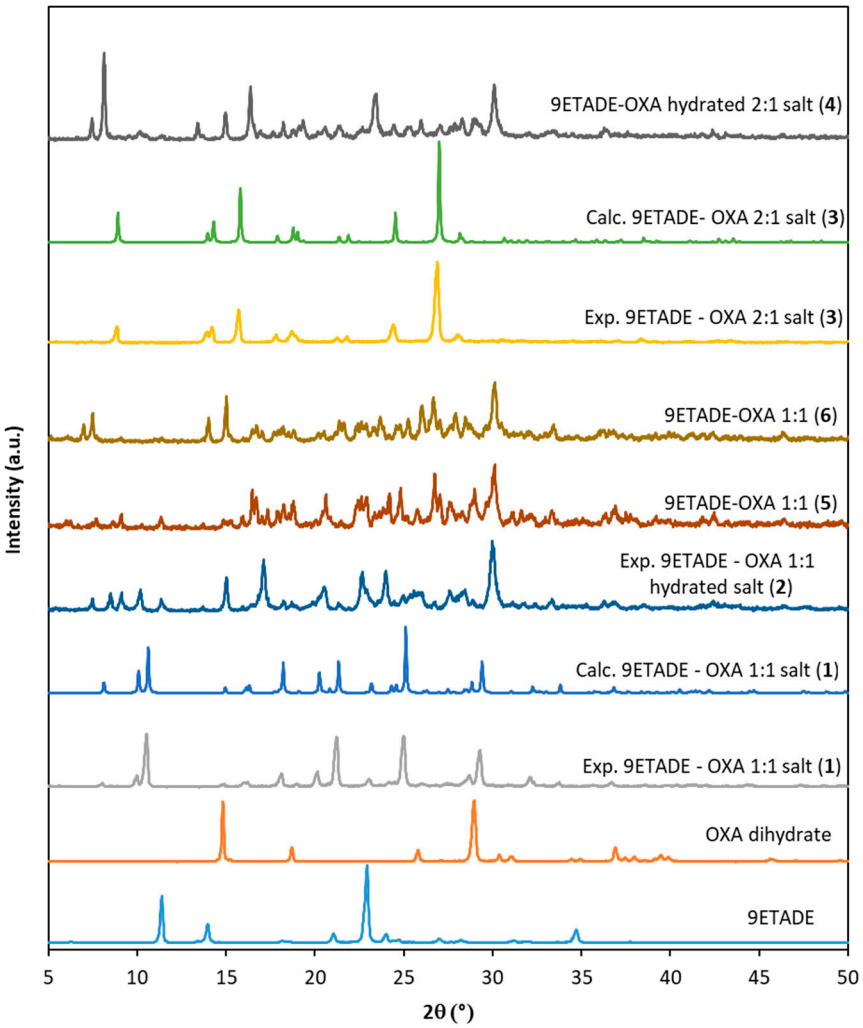

Figure 1. Comparison of the experimental and calculated powder patterns of 9ETADE, oxalic acid dihydrate and the as-synthesized compounds **1**–**6**.

During the mechanochemical screening, for the 2:1 molar ratio by NG or LAG in methanol or water, the powder patterns of the resulting solids were identical to the diffractogram of compound **4**. However, for the 1:1 ratio, the situation was much more complex. Use of water or methanol afforded powder patterns not only different between them but also to the ones obtained in solution with water or acetonitrile. The solid obtained by LAG in water was identified as compound **5** and the solids obtained by NG or by LAG in methanol, as compound **6**. The diffractograms of solids **5** and **6** are shown in Figure 1).

Between the powder patterns of solids **2** and **5** some differences can be observed, and therefore they will be treated as two different forms. Even if these two solid forms show

some characteristics in common not only in their FT-IR spectra but also in their TGA-DSC traces, as it will be commented below. Among all the other forms or respect to the starting products, characteristic and distinguished peaks are clearly observed. Furthermore, the agreement among the experimental and calculated patterns from single crystal data for compounds **1** and **3** was excellent. Surprisingly, the shortest dicarboxylic acid we used resulted the most fruitful in rendering different solid forms.

All the new compounds were analyzed by Fourier Transform Infrared spectroscopy in Attenuated Total Reflectance mode (ATR-FT-IR) and thermal methods (TGA-DSC) to elucidate the nature of these materials. Changes in the IR spectra of the new solids respect to the starting compounds have provided evidence that new H-bond interactions have taken place. Moreover, the presence or absence of several characteristic vibration modes, as for instance NH_2, COOH, C=N, gave further information of these new contacts. The IR spectra are included in Figure 2.

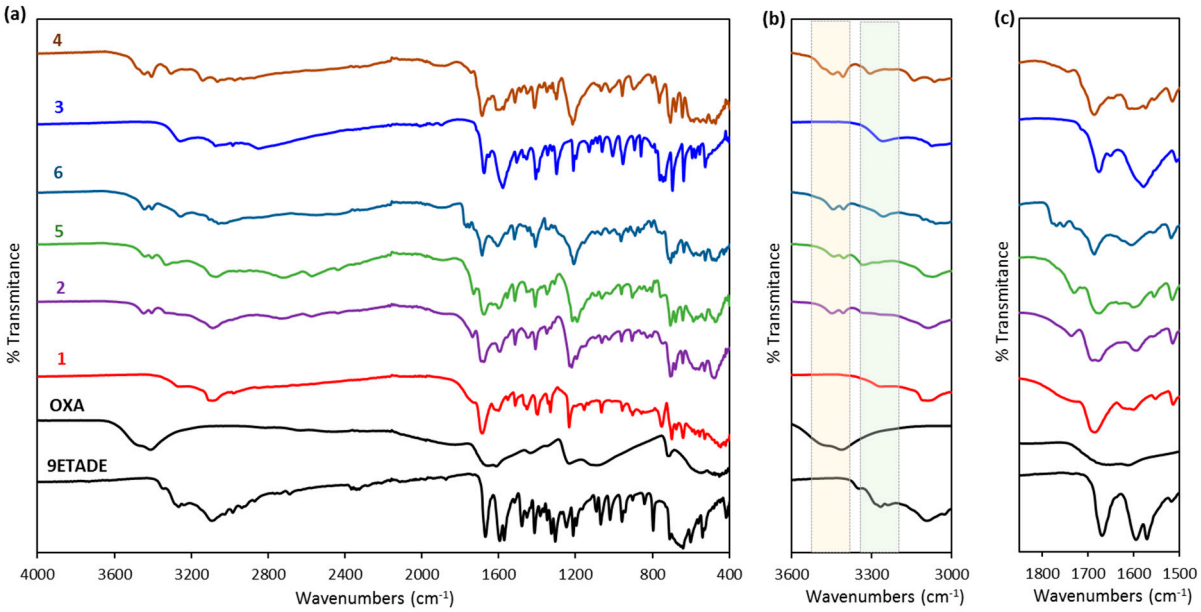

Figure 2. FT-IR spectra of (**a**) 9ETADE, oxalic acid dihydrate and the as-synthesized compounds in the full range, and in the ranges (**b**) 3600–3000 cm^{-1} or (**c**) 1850–1500 cm^{-1}.

The main difference among compounds prepared from aqueous slurries (**1** and **3**) with respect to all the others is the absence of one or two bands in the region 3450–3400 cm^{-1} (see Figure 2). While for these two solids no bands are observed, confirming the anhydrous state observed in the thermal analysis, for all the other compounds (**2**, **4**–**6**), two bands at ca. 3446 and 3407 cm^{-1} were present, which could be assigned to OH from water, and from the hydroxyl of unprotonated oxalic acid. Some differences in the NH region can be also detected.

In the spectra of the starting compounds, the also characteristic ν(C=O), ν(C=N), and δ_{sciss} (NH_2) vibrations appear at 1654, 1610 and 1669 cm^{-1}. For some of the compounds (**1**, **4** and **6**), only a broad band coincides at approximately at 1686 cm^{-1}, or for **3** and **5**, at 1678 cm^{-1}, in agreement with previous observations [9]. However, for the solid **2** a doublet overlapped band at 1694 and 1678 cm^{-1} can be detected. Moreover, for compounds **1**, **2** and **4**–**6**, a small band appears between 1728–1770 cm^{-1}, which confirms again the presence of C=O from unprotonated –COOH from oxalic acid [40]. No band is observed in this region for compound **3**.

By simultaneous thermogravimetric analysis (TGA)—differential scanning calorimetry/differential thermal analysis (DSC/DTA)—the stability of the new salts was evaluated. Both compounds **1** and **3** were anhydrous according to their TGA traces (Figures S1 and S2, respectively). In the DSC trace for compound **3** only one big endothermic peak correspond-

ing to the melting process (melting peak value of 227.5 °C) and concomitant degradation was observed. This is the highest melting point for the solid forms prepared in this work. Thus, this is the most stable form. For compound **1**, the DSC showed a previous small *endo* with an onset temperature of 176.2 °C followed by two overlapped endothermic processes with an onset temperature for the first one at 211.6 °C. The second endothermic peak (T_{peak}, 227.8 °C) agrees with the one observed for compound **3**. This event would suggest the loss of an oxalic acid molecule to achieve the salt **3** in 2:1 molar ratio.

On the contrary, compounds **2** and **4** showed each one a loss on drying (lod), of 2.74 and 4.19%, respectively, until 125 °C (Figures S3 and S4). They were assigned to dehydration processes of 1/3 to 1/2 of molecule of water for **2** (being probably a non-stoichiometric hydrated) and one molecule of water for **4** (theor. lod of one H_2O, 4.16%). In their DSC after these desolvation processes (at T_{peak} 107.2 °C for **2** and T_{peak}, 111.5 °C for **4**), the melting of the solids followed by degradation was observed.

The TGA-DSC trace for compound **5** resembles to the one of **2**. In its TGA a loss of 2.6% was observed closer to the theoretical value for a third hydrate compound (2.32%) and appeared in the same region. Besides, in the DSC an endothermic desolvation process was observed (peak temperature at 111.7 °C) and a subsequent melting (melting peak temperature, 187.9 °C) and its degradation (Figure S5).

Finally, for compound **6**, in the TGA trace a mass loss of about 5.8% was observed before complete degradation of the solid, suggesting that a new solvate was formed. The theoretical loss for a monohydrate solid form is 6.6%. The DSC thermogram showed several endothermic events, unveiling a complex desolvation process for this solid form (Figure S6).

3.2. Single-Crystal Structures

The crystal structures of compounds **1** and **3** were solved by single crystal X-ray diffraction. All trials performed to obtain suitable single crystals for the other multicomponent solids observed in this work were unfruitful. ORTEP images of both compounds are included in Figure S7.

9-Ethyladenine—oxalic acid (1:1) salt (**1**). Crystal structure analysis of compound **1** reveals that this compound crystallizes in the triclinic *P*-1 space group and the asymmetric unit consists of a protonated molecule of 9ETADE and a hydrogen oxalate anion. No solvent molecules are observed in agreement with its FTIR spectrum or the TGA trace where no loss on drying was observed before melting. Moreover, the agreement between the experimental and the simulated patterns for the 9ETADE-oxalic acid (1:1) salt is excellent indicating the high purity of the bulk solid obtained by slurry, Figure 1.

The structure consists of the self-assembly of two adenine moieties through its Hoogsteen edge by N(6)–H···N(7) interactions (distance: 2.9469(18) Å; angle 161.6°) forming a $R_2^2(10)$ motif (see Figure 3). Oxalate anions are connected head-to-tail through a strong hydrogen bond (distance: O(1B)–H(1B)···O(3B), 2.4728(15) Å). Furthermore, two molecules of 9ETADE interact with two hydrogen oxalate molecules through the NH_2 group and N(1) to the carboxylic acids of different oxalate anions, as follows: N(6A)–H···O(2B) (distance 2.9438(17) Å; angle 139.9°), N(6A)–H···O(3B) (distance 3.0271(18) Å; angle 128.7°), N(1A)–H···O(1B) (distance 3.0412(17) Å; angle 124.0(16)°) and N(1A)–H···O(4B) (distance 2.7449(16) Å; angle 158.7(18)°) following ring motifs $R_1^2(5)$, and a further C(2A)–H(2A)···O(1B) interaction.

The whole structure is formed by the connection of the layers formed by 9ETADE dimers and hydrogen oxalate ions (Figure 3c) through the hydrogen bonds, as follows: C(10A)–H(10A)···O(4B) and C(8A)–H(8A)···O(2A). The complete list of H-bonding interactions is shown in Table S1.

9-Ethyladenine—oxalic acid (2:1) salt (**3**). Single crystals of this salt were obtained by slow evaporation of a mixture in acetonitrile—water (1:1 vol/vol). In this case, 9ETADE and oxalic acid crystallize in the monoclinic $P2_1/c$ space group containing two protonated molecules of 9ETADE and an oxalate anion in the asymmetric unit forming a salt in a 2:1

ratio. No solvent molecules are observed, again in agreement with the TGA trace or the FTIR spectrum.

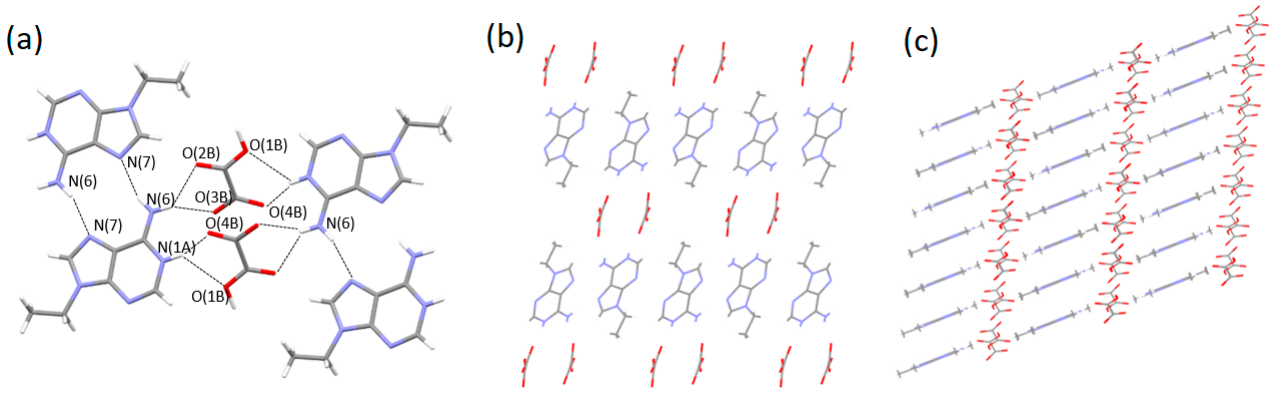

Figure 3. (**a**) Hydrogen bonding interactions, (**b**) layers (view along *a* axis) and (**c**) view along the vector (−2 1 0) in compound **1** (9ETADE-OXA (1:1) salt).

Two molecules of 9ETADE are bridged by an oxalate molecule through the following interactions (Figure 4): N(6A)–H···O(2B) (distance 2.743(3) Å; angle 152.7°), N(1A)–H···O(1B) (distance 2.746(3) Å; angle 148(3)°) and N(1A)–H···O(2B) (distance 2.968(3) Å; angle 133(3)°). An additional hydrogen bond to a second oxalate anion is established through N(6A)–H···O(1B) (distance 2.873(3) Å; angle 156.4°), thus constituting belts perpendicular to the **c** axis. These belts are pilled by hydrogen bonds through the methyl group from the ethyl chain to the carbonyl from the oxalate anion (distance C(11A)–H(11A)···O(2B), 3.576(5) Å). Among 9-ethyladenine molecules, only C–H···N contacts are observed (C(2A)–H(2A)···N(7A), 3.224(4) Å). Surprisingly, the N(7A)–Cg distance (3.398 Å) is shorter than the distance between mean planes for two pilled 9ETADE molecules, suggesting an attractive lone pair–π interaction (N(7A)···6-membered ring). The complete list of hydrogen bonds is included in the Supplementary Information, Table S2.

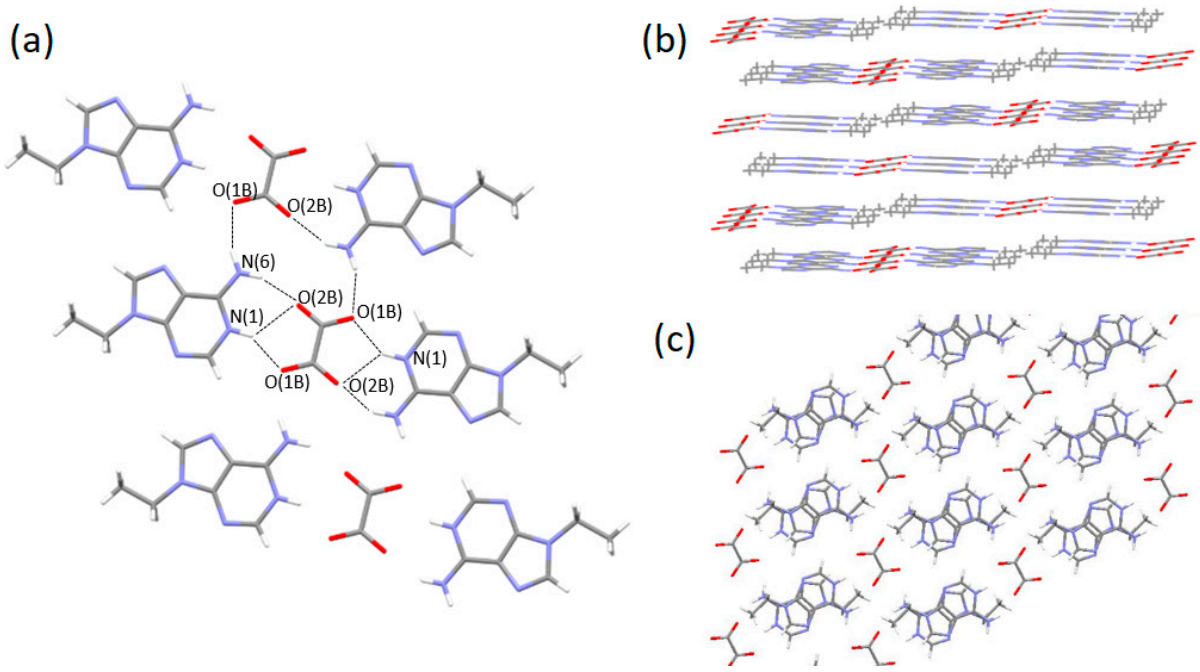

Figure 4. (**a**) Hydrogen bonds and (**b**) packing of the belts (view along the *b* axis, slightly tilted to improve the perspective) and (**c**) π–π stacking (view along the *c* axis) in 9ETADE-oxalic acid (2:1) salt (**3**).

The agreement between the experimental and the simulated powder diffraction patterns for the 9ETADE-oxalic acid (2:1) salt is excellent, Figure 1.

Although the crystal structures for the other multicomponent solids shown in this work were unavailable, the data collected from IR spectroscopy, thermogravimetric analyses, and the knowledge from previous crystal structures regarding to other salts and cocrystals described for this compound allow to determine their composition. So, we hypothesize that compound **4** contains a half double charge oxalate anion and a half unprotonated oxalic acid molecule per 9ETADE molecule. Additionally, for compounds **2**, **5** and **6**, a half mono-oxalate anion and a half unprotonated oxalic acid should be present, although with different contents of water molecules in each case.

3.3. Aqueous Solubilities

One of the main objectives of conducting salt/cocrystal screenings of active molecules is to find suitable candidates with the best physical-chemical properties. In a previous work, we described two new hydrated salts (malonate and fumarate) and an anhydrous succinate of 9ETADE [18]. Herein, the aqueous solubilities of 9-ethyladenine and the three anhydrous candidates (the two anhydrous oxalate salts prepared in this work and the succinate salt of 9ETADE) were determined for comparative purposes (Table 2).

Table 2. Aqueous solubilities of the succinate salt, compounds **1** and **3** and the precursors.

Compound	Solubility (mg/mL)	Coformer	Solubility * (mg/mL)
9ETADE	533		
9ETADE-OXA (1:1) salt (**1**)	25	Oxalic acid dihydrate	100
9ETADE-OXA (2:1) salt (**3**)	10		
9ETADE-SUC (1:1) salt	7	Succinic acid	83

* Sigma-Aldrich.

From these results, the modified nucleobase showed the highest solubility in water in comparison to the other salts or even the former carboxylic acids used. Although the results did not indicate an improvement in the solubility behavior of the new compounds, it shows that it is possible to modulate this property, resulting apparently the 9ETADE-OXA (1:1) solid form the most soluble of the three studied salts.

The undissolved residues were analyzed by PXRD. It is worth noting that the compound **1** had transformed partially to the 2:1 salt, compound **3**. Thus, this case is a new example of a solvent-mediated phase transformation and the solubility value obtained for this compound should be discarded. Nevertheless, the results obtained indicated that the powder patterns for this compound **3** and the succinate (1:1) salt remained undisturbed (Figure S8).

3.4. Stability Studies in Solution and Solid State

In order to understand the phase stability of the multicomponent forms in 1:1 molar ratio in solution, the process was investigated over time by PXRD. After 2 h, either using water or acetonitrile resulted to be almost undistinguished products, as the XRD patterns were quite similar. However, the slurry in water after 24 h contained a mixture of the previous phase and a new one, which resulted the unique after 48 h and matched with the diffractogram obtained for compound **1** (Figure 5, below). For the mixture in acetonitrile, the phase transformation was also detected by the presence of new peaks in the powder pattern after stirring for 24 h, which after 48 h resulted in the same PXRD as for compound **2**.

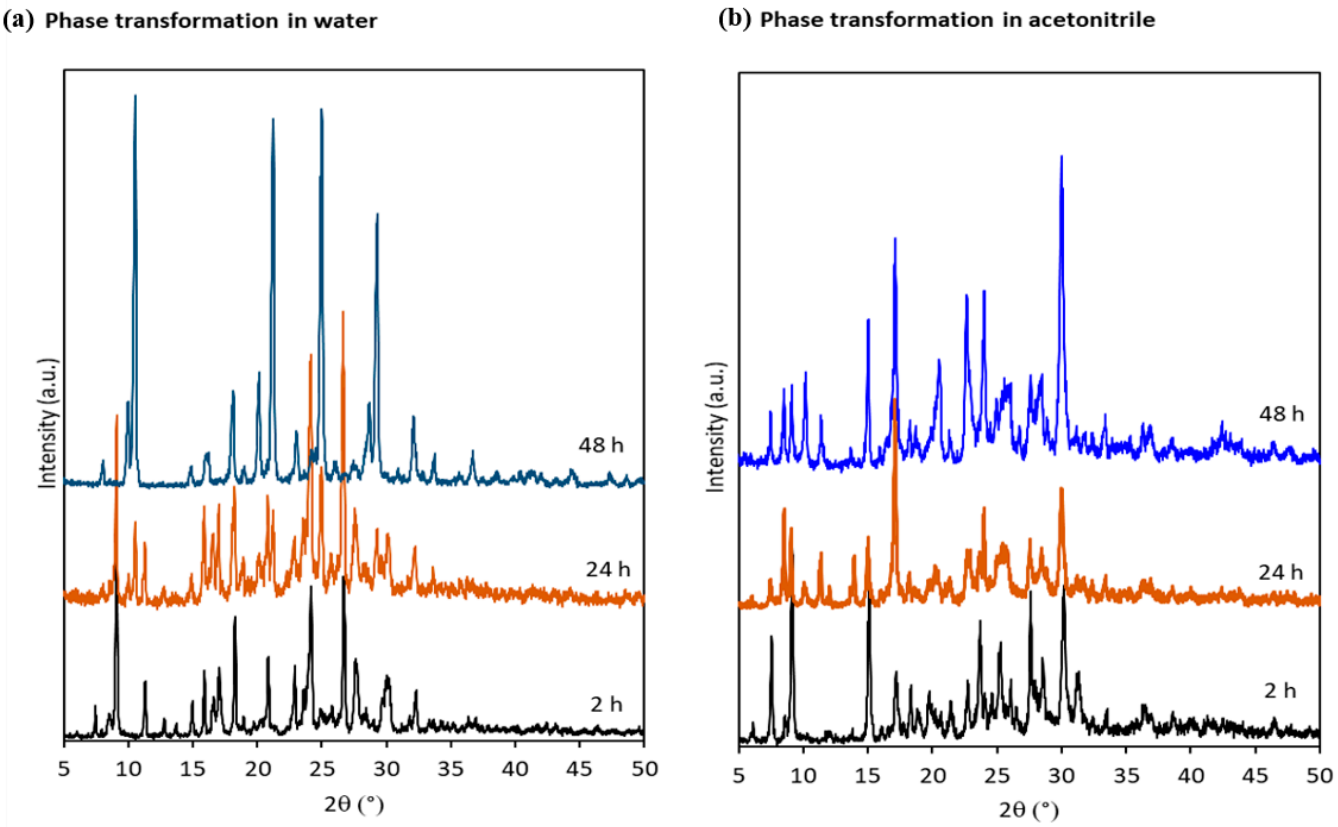

Figure 5. Phase transformations in slurry experiments in (**a**) water or (**b**) in acetonitrile.

Furthermore, the physical stability of the anhydrous oxalate salts against humidity was studied. These solids were stored in a desiccator at 75% RH using a saturated NaCl salt solution for 7 days at 40 °C and for 1 month at room temperature. After these periods the solids were again analyzed by PXRD to confirm the phase of the solids. The analysis of the solids indicated that both anhydrous oxalate salts were stable under the two stability conditions tested (Figure S9).

3.5. Computational Studies

The theoretical study is firstly focused on analyzing electronic nature of the 9ETADE ring and, more importantly, how changes upon protonation and formation of the corresponding salts with hydrogenoxalate and oxalate. Secondly, we have evaluated the H-bonding networks that are formed in the solid state of compounds **1** and **3**, as described above in Figures 3a and 4a.

Figure 6 shows the MEP surfaces of 9ETADE and its salts. In neutral 9ETADE, the MEP minimum is located at N1 (see Scheme 1a for numbering of atoms) in line with the protonation site observed in compounds **1** and **3**. The MEP values at N3 and N7 are similar (–25.1 and –24.7 kcal/mol, respectively). The MEP maximum is located at the exocyclic NH_2 group (+26.9 kcal/mol). The MEP is also large and positive (+20.0 kcal/mol) at the aromatic CH group of the five membered ring. The MEP surface of the 9-ethyladeninium–hydrogenoxalate salt extracted from the solid state of compound **1** is represented in Figure 6b. The protonation increases the MEP values at the NH_2 (+59.8 kcal/mol) and CH (+48.9 kcal/mol) groups with respect to the neutral 9ETADE, as expected. It is interesting to note that the MEP at the OH group is large and positive, despite the negative charge of hydrogenoxalate moiety. The MEP minimum is located at the O-atom of hydrogenoxalate (–81.6 kcal/mol). For the 9-ethyladeninium oxalate salt (Figure 6c), the MEP minimum is located at the oxalate anion, as expected (–77.2 kcal/mol) and the maximum at the exocyclic NH_2 group (+36.7 kcal/mol). It is worth mentioning that in this salt, the MEP value at the

CH group of the five membered ring is very large, similar to that at the NH_2 group, thus revealing an enhanced ability to establish H-bonds, as further discussed below.

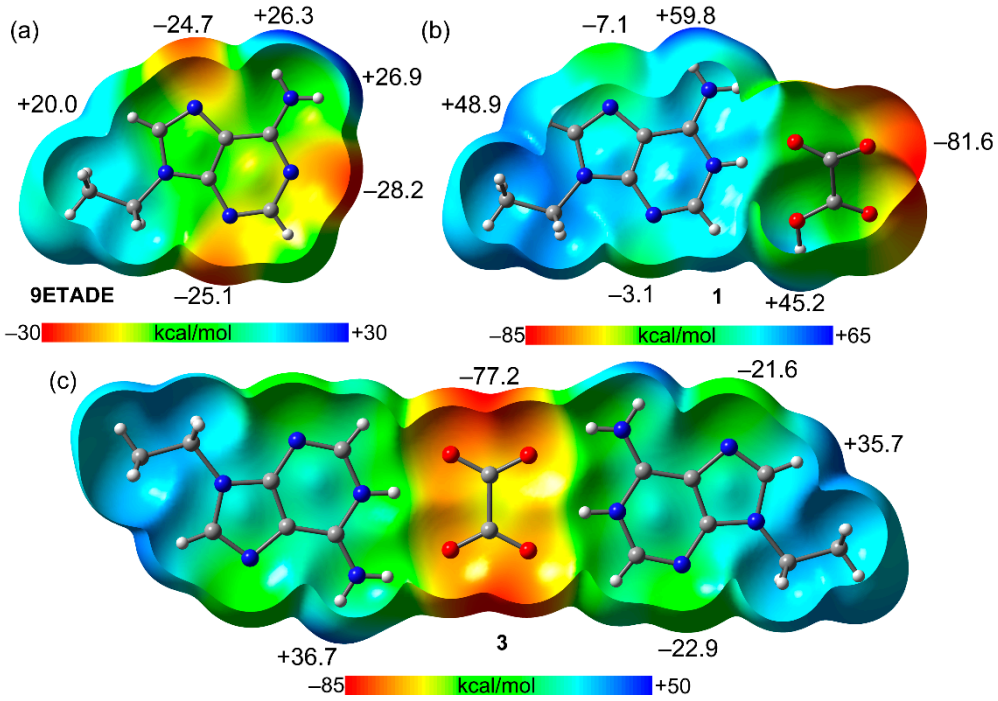

Figure 6. MEP surfaces (isovalue 0.01 a.u.) of 9ETADE (**a**), 9-ethyldeninimum hydrogenoxalate salt (**b**) and 9-ethyldeninimum oxalate salt (**c**) at the PBE0-D3/def2-TZVP level of theory. The energies at selected points of the surfaces are given in kcal/mol.

In the solid state of compound **1**, the protonated 9ETADE rings form centrosymmetric $R_2^2(10)$ H-bonded synthons, as highlighted in Figure 7, which are surrounded by four hydrogenoxalate monoanions (see Section 3.2 for distances and other geometric features). The distribution of bond and ring critical points (CPs, red and yellow spheres, respectively) and bond paths is represented in Figure 7 for the whole assembly, where the superimposed noncovalent interaction plot (NCIPlot) index isosurfaces are also represented. The NCIplot index method is conveniently used to characterize noncovalent interactions in real space. It also reveals the attractive or repulsive nature of the interactions by using a color scale. The QTAIM distribution shows that the two symmetrically equivalent N6–H7···N7 bonds that generate the $R_2^2(10)$ synthon are characterized by bond CPs and bond paths connecting the H-atoms to the N-atoms. Moreover, they are also characterized by small and blue NCIplot isosurfaces, revealing a moderately strong interaction. The formation of this assembly agrees well with the MEP analysis commented above that evidences the strong H-bond donor ability of the NH_2 group in the salts. The dissociation energy of each individual H-bond has been computed using the potential energy density values at the bond CPs (V_r) and the equation proposed by Espinosa et al. ($E_{dis} = -0.5 \times V_r$) [39]. The E_{dis} values are indicated in Figure 7 next to the bond CPs in red, showing that the binding energy of the $R_2^2(10)$ synthon is 7.8 kcal/mol, in line with other studies related to the energetics of Hoogsteen base pair [41,42]. Regarding the H-bonds of the $R_2^2(10)$ dimer with the counterions, the combined QTAIM/NCIplot analysis shows a quite intricate H-bonding network where each hydrogenoxalate anion establishes three H-bonds with the base pair, each one characterized by the corresponding bond CP and bond path. The strongest one corresponds to the charge assisted H-bond ($N1^+$–H···O, 7.3 kcal/mol) and the rest of H···O contacts range from 1.4 to 2.6 kcal/mol. In line with the MEP surface analysis, the CH group also participates in the H-bonding network with a moderately strong interaction energy (2.4 kcal/mol), comparable to other NH···O contacts. The total dissociation energy is

42.4 kcal/mol, thus evidencing the importance of the H-bonding network on the solid-state architecture of compound **1**.

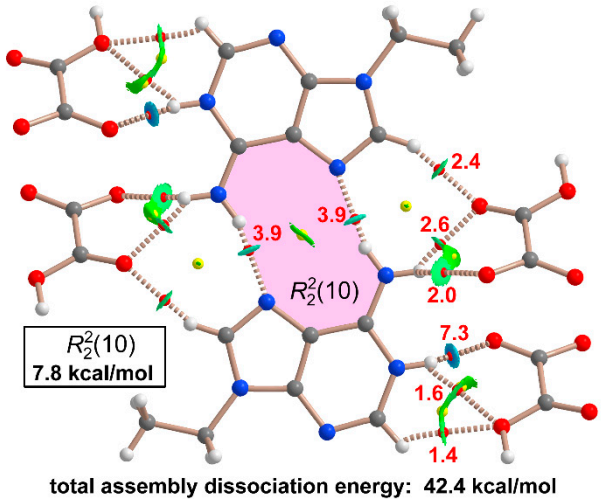

Figure 7. QTAIM distribution of bond and ring critical points (CPs, red and yellow spheres, respectively) corresponding to the H-bonds in the $R_2{}^2(10)$ synthons and its interaction with four surrounding $[C_2O_4H]^-$ anions. The dissociation energies of the H-bonds are indicated next to the bond CPs. Superimposed NCIplot isosurfaces [s = 0.5, cut-off = 0.04 a.u., color scale –0.04 a.u. (blue) $\leq$ (signλ_2)$\rho \leq$ 0.04 a.u. (red)] are also represented.

In the literature, the ability of adenine derivatives and cocrystals to form $R_2{}^2(10)$ homodimers or a variety of heterodimers via the Hoogsteen face has been described and energetically evaluated using the QTAIM analysis [41–43]. For instance, the reported energies associated with NH···N H-bonds in $R_2{}^2(10)$ ethyl-adenine homodimers in its co-crystals with malonic and fumaric acid are 3.6 and 4.0 kcal/mol [18], respectively. These values are comparable to those obtained for compound **1**. Similar interaction energies have been also reported for Hoogsteen (adenine)· · · Watson–Crick (N^7-pyrimidyladenine) heterodimers (3.7 and 4.2 kcal/mol) [44].

Figure 8 shows a similar QTAIM/NCIplot analysis performed for compound **3**. In this case, the $R_2{}^2(10)$ synthon via the Hoogsteen face is not formed. Each oxalate anion is surrounded by four 9-ethyladeninium cations establishing a network of H-bonding, characterized by the corresponding bond CPs, bond paths and blue NCIplot isosurfaces. The individual dissociated energies shown in Figure 8 reveal that two strong H-bonds are formed. One corresponds to the charge assisted HB ($N1^+$–H···O, 7.1 kcal/mol) and the other one corresponds to the N6–H6···O H-bond (6.1 kcal/mol) formed through the Watson–Crick face. The N6–H6···O H-bond formed through the Hoogsteen face is weaker (4.5 kcal/mol). These values are comparable to previously reported energies for adenine co-crystals with several carboxylic acids [18]. The QTAIM analysis also reveals the existence of a much weaker H-bond established between the aromatic CH bond of the six membered ring and N7 (2.0 kcal/mol), in line with the MEP surface plot depicted in Figure 6c. The total dissociation energy of this H-bonding network is very large (40.0 kcal/mol), specially taking into consideration that involves only one oxalate dianion, thus providing a great stability to compound **3**.

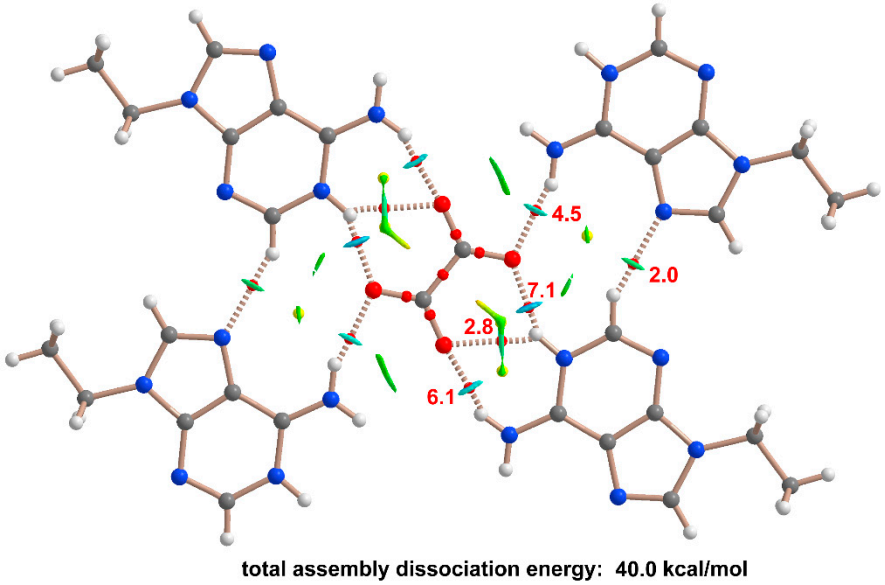

Figure 8. QTAIM distribution of bond and ring critical points (CPs, red and yellow spheres, respectively) corresponding to the pentameric assembly of compound **3**. The dissociation energies of the H-bonds are indicated next to the bond CPs. Superimposed NCIplot isosurfaces [s = 0.5, cut-off = 0.04 a.u., color scale −0.04 a.u. (blue) $\leq$ (signλ_2)$\rho \leq$ 0.04 a.u. (red)] are also represented.

4. Concluding Remarks

The mixture of 9-ethyladenine and oxalic acid have, surprisingly, resulted in the most productive nucleobase or derivative up to the authors' knowledge. For most of the studied nucleobases or their derivatives found in the literature (adenine, n-benzyladenine, caffeine, theobromine, theophylline or even lamivudine), the salt/cocrystal in a 2:1 ratio is the most common solid form. In this work, we have described up to six different multicomponent solids including two molar ratios and anhydrous/solvated forms using mechanochemistry, slurry or crystallization experiments. Once again, it reflects the importance of the combination of all these techniques as complementary tools besides to computational methods to fully understand the solid state landscape of multicomponent pharmaceutical solids for a determined API or model compound.

The obtained solids have been characterized and the crystal structures for the two anhydrous forms have been solved. The H-bonding networks observed in the solid-state of both compounds have been analyzed using DFT calculations combined with the QTAIM methodology. The energy of each individual H-bond has been computed, showing the relevance of the $R_2^2(10)$ centrosymmetric dimer in **1**. The dissociation energies of the charge assisted H-bonds ($N1^+$–H···O) are similar in both compounds, which are the strongest H-bonds (~7 kcal/mol) formed in the solid state. The QTAIM analysis also evidences the relevance of CH···O interactions (up to 2.4 kcal/mol) as ancillary interactions in both compounds.

Supplementary Materials: The following are available online at https://www.mdpi.com/article/10.3390/cryst12010089/s1, Experimental methods for solution syntheses and grinding screening. Figure S1: TGA-DSC traces of 9-ethyladenine-oxalic acid (1:1) salt (1). Figures S2: TGA-DSC traces of 9-ethyladenine-oxalic acid (2:1) salt (3). Figure S3: TGA-DSC traces of 9-ethyladenine-oxalic acid hydrated (1:1) salt (2). Figure S4: TGA-DSC traces of 9-ethyladenine-oxalic acid hydrated salt (4). Figures S5: TGA-DSC traces of 9-ethyladenine-oxalic acid hydrated (1:1) salt (5). Figure S6: TGA-DSC traces of 9-ethyladenine-oxalic acid hydrated (1:1) hydrated salt (6). Figure S7: Ortep images of compounds (a) 1 and (b) 3. Table S1: Hydrogen bond details for 9-ethyladenine-oxalic acid (1:1) salt (1). Table S2: Hydrogen bond details for 9-ethyladenine-oxalic acid (2:1) salt (3). Figure S8: Diffractograms of initial and undissolved solids for compounds 9ETADE-OXA (2:1) (3), 9ETADE-

OXA (1:1) (1) and 9ETADE-SUC (1:1) salt. Figure S9: PXRD patterns of the anhydrous 9ETADE-OXA salts under different temperature and relative humidity conditions.

Author Contributions: M.B.-O. prepared 9-ethyladenine. M.B. designed the experiments, characterized the samples and obtained the single crystals. M.B.-O. performed the data collection and the resolution of the crystal structures. A.F. performed the D.F.T. study. M.B., A.F. and E.M. designed the concept. E.M. supervised the work. All authors wrote and revised the manuscript. All authors have read and agreed to the published version of the manuscript.

Funding: M.B. and E.M. are grateful to the Severo Ochoa FunFuture project (MICINN, CEX2019-917S) and Generalitat de Catalunya (2017SGR1687). M.B.-O. thanks the Vice-Rector for Research and International Relations of the University of the Balearic Islands for the financial support in setting up the single-crystal X-ray diffraction facility. A.F. thanks the MICIU/AEI from Spain for financial support (Projects CTQ2017-85821-R and PID2020-115637GB-I00, Feder funds).

Institutional Review Board Statement: Not applicable.

Informed Consent Statement: Not applicable.

Data Availability Statement: Not applicable.

Acknowledgments: We thank R. Frontera from the Centre de Tecnologies de la Informació (CTI) at the UIB for computational facilities. The authors also thank the powder diffraction and thermal analysis services from the ICMAB.

Conflicts of Interest: The authors declare no conflict of interest.

References

1. Stahl, P.H.; Wermuth, C.G. (Eds.) *Handbook of Pharmaceutical Salts: Properties, Selection and Use*; Wiley-VCH: Zurich, Switzerland, 2008.
2. Harrison, W.T.A.; Yathirajan, H.S.; Bindya, S.; Anilkumar, H.G. Devaraju Escitalopram oxalate: Co-existence of oxalate dianions and oxalic acid molecules in the same crystal. *Acta Crystallogr. Sect. C Cryst. Struct. Commun.* **2007**, *63*, o129–o131. [CrossRef]
3. Åaslund, B.L.; Aurell, C.J.; Bohlin, M.H.; Sebhatu, T.; Ymen, B.I.; Healy, E.T.; Jensen, D.R.; Jonaitis, D.T.; Parent, S. Crystalline Naloxol-Peg Conjugate. Patent WO2012044243A1, 5 April 2012.
4. Gelbrich, T.; Langes, C.; Stefinovic, M.; Griesser, U.J. Naloxegol hydrogen oxalate displaying a hydrogen-bonded layer structure. *Acta Crystallogr. Sect. E Crystallogr. Commun.* **2018**, *74*, 474–477. [CrossRef] [PubMed]
5. Paulekuhn, G.S.; Dressman, J.B.; Saal, C. Trends in Active Pharmaceutical Ingredient Salt Selection based on Analysis of the Orange Book Database. *J. Med. Chem.* **2007**, *50*, 6665–6672. [CrossRef] [PubMed]
6. Owoyemi, B.C.D.; da Silva, C.C.P.; Diniz, L.F.; Souza, M.S.; Ellena, J.; Carneiro, R.L. Fluconazolium oxalate: Synthesis and structural characterization of a highly soluble crystalline form. *CrystEngComm* **2019**, *21*, 1114–1121. [CrossRef]
7. Chen, Y.; Li, L.; Yao, J.; Ma, Y.-Y.; Chen, J.-M.; Lu, T.-B. Improving the Solubility and Bioavailability of Apixaban via Apixaban–Oxalic Acid Cocrystal. *Cryst. Growth Des.* **2016**, *16*, 2923–2930. [CrossRef]
8. Dichiarante, E.; Curzi, M.; Giaffreda, S.L.; Grepioni, F.; Maini, L.; Braga, D. Crystal forms of the hydrogen oxalate salt of o-desmethylvenlafaxine. *J. Pharm. Pharmacol.* **2015**, *67*, 823–829. [CrossRef]
9. Perumalla, S.R.; Sun, C.C. Design and Preparation of a 4:1 Lamivudine–Oxalic Acid CAB Cocrystal for Improving the Lamivudine Purification Process. *Cryst. Growth Des.* **2014**, *14*, 3990–3995. [CrossRef]
10. Available online: https://www.fda.gov/news-events/press-announcements/fda-hold-advisory-committee-meeting-discuss-merck-and-ridgebacks-eua-application-covid-19-oral (accessed on 1 December 2021).
11. Sridhar, B.; Ravikumar, K.; Varghese, B. Supramolecular hydrogen-bonded networks in adeninediium hemioxalate chloride and adeninium semioxalate hemi(oxalic acid) monohydrate. *Acta Crystallogr. Sect. C Cryst. Struct. Commun.* **2009**, *65*, o202–o206. [CrossRef]
12. McHugh, C.; Erxleben, A. Supramolecular Structures and Tautomerism of Carboxylate Salts of Adenine and Pharmaceutically Relevant N6-Substituted Adenine. *Cryst. Growth Des.* **2011**, *11*, 5096–5104. [CrossRef]
13. Trask, A.V.; Motherwell, W.D.S.; Jones, W. Pharmaceutical Cocrystallization: Engineering a Remedy for Caffeine Hydration. *Cryst. Growth Des.* **2005**, *5*, 1013–1021. [CrossRef]
14. Otsuka, Y.; Ito, A.; Takeuchi, M.; Tanaka, H. Dry Mechanochemical Synthesis of Caffeine/Oxalic Acid Cocrystals and Their Evaluation by Powder X-ray Diffraction and Chemometrics. *J. Pharm. Sci.* **2017**, *106*, 3458–3464. [CrossRef] [PubMed]
15. Fischer, F.; Scholz, G.; Batzdorf, L.; Wilke, M.; Emmerling, F. Synthesis, structure determination, and formation of a theobromine: Oxalic acid 2:1 cocrystal. *CrystEngComm* **2014**, *17*, 824–829. [CrossRef]
16. Zhang, S.; Rasmuson, C. The theophylline–oxalic acid co-crystal system: Solid phases, thermodynamics and crystallisation. *CrystEngComm* **2012**, *14*, 4644–4655. [CrossRef]
17. Trask, A.V.; Motherwell, W.D.S.; Jones, W. Physical stability enhancement of theophylline via cocrystallization. *Int. J. Pharm.* **2006**, *320*, 114–123. [CrossRef]

18. Roselló, Y.; Benito, M.; Bagués, N.; Martínez, N.; Moradell, A.; Mata, I.; Galcerà, J.; Barceló-Oliver, M.; Frontera, A.; Molins, E. 9-Ethyladenine: Mechanochemical Synthesis, Characterization, and DFT Calculations of Novel Cocrystals and Salts. *Cryst. Growth Des.* **2020**, *20*, 2985–2997. [CrossRef]
19. García-Raso, A.; Fiol, J.J.; Bádenas, F.; Solans, X.; Font-Bardia, M. Reaction of trimethylene–bisadenine with d10 divalent cations. *Polyhedron* **1999**, *18*, 765–772. [CrossRef]
20. *SADABS, Bruker-AXS*; Version 1; Bruker AXS Inc.: Madison, WI, USA, 2004.
21. Farrugia, L.J. WinGX suite for small-molecule single-crystal crystallography. *J. Appl. Crystallogr.* **1999**, *32*, 837–838. [CrossRef]
22. Sheldrick, G.M. Crystal structure refinement with SHELXL. *Acta Crystallogr.* **2015**, *C71*, 3–8. [CrossRef]
23. Sheldrick, G.M. *SHELXL-2017/1, Program for the Solution of Crystal Structures*; University of Göttingen: Göttingen, Germany, 2017.
24. Spek, A.L. Structure validation in chemical crystallography. *Acta Crystallogr.* **2009**, *D65*, 148–155. [CrossRef]
25. Ahuja, D.; Svärd, M.; Rasmuson, C. Investigation of solid–liquid phase diagrams of the sulfamethazine–salicylic acid co-crystal. *CrystEngComm* **2019**, *21*, 2863–2874. [CrossRef]
26. Alvarez-Lorenzo, C.; Castiñeiras, A.; Frontera, A.; García-Santos, I.; González-Pérez, J.M.; Niclós-Gutiérrez, J.; Rodríguez-González, I.; Vílchez-Rodríguez, E.; Zaręba, J.K. Recurrent motifs in pharmaceutical cocrystals involving glycolic acid: X-ray characterization, Hirshfeld surface analysis and DFT calculations. *CrystEngComm* **2020**, *22*, 6674–6689. [CrossRef]
27. Rockland, L.B. Saturated Salt Solutions for Static Control of Relative Humidity between 5° and 40° C. *Anal. Chem.* **1960**, *32*, 1375–1376. [CrossRef]
28. Frisch, M.J.; Trucks, G.W.; Schlegel, H.B.; Scuseria, G.E.; Robb, M.A.; Cheeseman, J.R.; Scalmani, G.; Barone, V.; Mennucci, B.; Petersson, G.A.; et al. *Gaussian16*; Revision A.03; Gaussian Inc.: Wallingford, CT, USA, 2016.
29. Adamo, C.; Barone, V. Toward reliable density functional methods without adjustable parameters: The PBE0 model. *J. Chem. Phys.* **1999**, *110*, 6158–6170. [CrossRef]
30. Grimme, S.; Antony, J.; Ehrlich, S.; Krieg, H. A consistent and accurate ab initio parametrization of density functional dispersion correction (DFT-D) for the 94 elements H-Pu. *J. Chem. Phys.* **2010**, *132*, 154104. [CrossRef] [PubMed]
31. Weigend, F. Accurate Coulomb-fitting basis sets for H to Rn. *Phys. Chem. Chem. Phys.* **2006**, *8*, 1057–1065. [CrossRef] [PubMed]
32. Gomila, R.M.; Frontera, A. Metalloid Chalcogen–pnictogen σ-hole bonding competition in stibanyl telluranes. *J. Organomet. Chem.* **2021**, *954–955*, 122092. [CrossRef]
33. Mertsalov, D.F.; Gomila, R.M.; Zaytsev, V.P.; Grigoriev, M.S.; Nikitina, E.V.; Zubkov, F.I.; Frontera, A. On the Importance of Halogen Bonding Interactions in Two X-ray Structures Containing All Four (F, Cl, Br, I) Halogen Atoms. *Crystals* **2021**, *11*, 1406. [CrossRef]
34. García-Rubiño, M.; Matilla-Hernández, A.; Frontera, A.; Lezama, L.; Niclós-Gutiérrez, J.; Choquesillo-Lazarte, D. Dicopper(II)-EDTA Chelate as a Bicephalic Receptor Model for a Synthetic Adenine Nucleoside. *Pharmaceuticals* **2021**, *14*, 426. [CrossRef]
35. Le, A.T.; Tran, V.T.T.; Le, D.T.; Gomila, R.M.; Frontera, A.; Zubkov, F.I. Synthesis, X-ray characterization and theoretical study of all-cis 1,4:2,3:5,8:6,7-tetraepoxynaphthalenes: On the importance of the through-space α-effect. *CrystEngComm* **2021**, *23*, 7462–7470. [CrossRef]
36. Bader, R.F.W. A Bond Path: A Universal Indicator of Bonded Interactions. *J. Phys. Chem. A* **1998**, *102*, 7314–7323. [CrossRef]
37. Contreras-Garcia, J.; Johnson, E.R.; Keinan, S.; Chaudret, R.; Piquemal, J.-P.; Beratan, D.; Yang, W. NCIPLOT: A Program for Plotting Noncovalent Interaction Regions. *J. Chem. Theory Comput.* **2011**, *7*, 625–632. [CrossRef] [PubMed]
38. Keith, T.A. *AIMALL*; Version 19.10.12; TK Gristmill Software: Overland Park, KS, USA, 2019.
39. Espinosa, E.; Molins, E.; Lecomte, C. Hydrogen bond strengths revealed by topological analyses of experimentally observed electron densities. *Chem. Phys. Lett.* **1998**, *285*, 170–173. [CrossRef]
40. Carvalho, P.S.; Diniz, L.F.; Tenorio, J.C.; Souza, M.S.; Franco, C.H.J.; Rial, R.; De Oliveira, K.R.W.; Nazario, C.E.D.; Ellena, J. Pharmaceutical paroxetine-based organic salts of carboxylic acids with optimized properties: The identification and characterization of potential novel API solid forms. *CrystEngComm* **2019**, *21*, 3668–3678. [CrossRef]
41. García-Raso, A.; Terrón, A.; López-Zafra, A.; García-Viada, A.; Barta, A.; Frontera, A.; Lorenzo, J.; Rodríguez-Calado, S.; Vázquez-López, E.M.; Fiol, J.J. Crystal structures of N6-modified-amino acid related nucleobase analogs (II): Hybrid adenine-β-alanine and adenine-GABA molecules. *New J. Chem.* **2019**, *43*, 9680–9688. [CrossRef]
42. García-Raso, A.; Terrón, A.; Bauzá, A.; Frontera, A.; Molina, J.J.; Vázquez-López, E.M.; Fiol, J.J. Crystal structures of N6-modified-aminoacid/peptide nucleobase analogs: Hybrid adenine-glycine and adenine-glycylglycine molecules. *New J. Chem.* **2018**, *42*, 14742–14750. [CrossRef]
43. García-Raso, A.; Terrón, A.; Balle, B.; López-Zafra, A.; Frontera, A.; Barceló-Oliver, M.; Fiol, J.J. Crystal structures of N6-modified-amino acid nucleobase analogs(iii): Adenine-valeric acid, adenine-hexanoic acid and adenine-gabapentine. *New J. Chem.* **2020**, *44*, 12236–12246. [CrossRef]
44. Martínez, D.; Pérez, A.; Cañellas, S.; Silió, I.; Lancho, A.; García-Raso, A.; Fiol, J.J.; Terrón, A.; Barceló-Oliver, M.; Orte-ga-Castro, J.; et al. Synthesis, reactivity, X-ray characterization and docking studies of N7/N9-(2-pyrimidyl)-adenine derivatives. *J. Inorg. Biochem.* **2020**, *203*, 110879. [CrossRef]